Article:
Rauter, P, Lin, J, Genevet, P et al. (5 more authors) (2014) Electrically pumped semiconductor laser with monolithic control of circular polarization. Proceedings of the National Academy of Sciences of USA, 111 (52). E5623-E5632. ISSN 1091-6490

https://doi.org/10.1073/pnas.1421991112

Electrically pumped semiconductor laser with monolithic control of circular polarization

Patrick Rauter[a], Jiao Lin[a], Patrice Genevet[a], Suraj P. Khanna[b], Mohammad Lachab[b], A. Giles Davies[b], Edmund H. Linfield[b], and Federico Capasso[a,1]

[a]School of Engineering and Applied Sciences, Harvard University, Cambridge, MA 02138, USA
[b]School of Electronic and Electrical Engineering, University of Leeds, Leeds, LS2 9JT, United Kingdom
[1]To whom correspondence may be addressed. E-mail: capasso@seas.harvard.edu

Author contributions: P.R., J.L., and F.C. designed research; P.R. performed research; S.P.K., M.L., A.G.D., and E.H.L. provided the QCL material. P.R., P.G., and F.C. analyzed data; and P.R., P.G., and F.C. wrote the paper.

Significance

As powerful semiconductor laser sources open up new possibilities for the realization of compact and versatile spectroscopy and detection systems, monolithic control of the laser output characteristics becomes essential. Whereas engineering of spectral characteristics and beam shape has reached a high level of maturity, manipulation of the polarization state remains challenging. We present a method for monolithic control of the degree of circular polarization by aperture antennas forming a surface-emitting grating on a semiconductor laser cavity and demonstrate its realization for a terahertz quantum cascade laser. Our approach is not limited to the terahertz regime and paves the way to an increased functionality and customizability of monolithic laser sources for a variety of applications (e.g., vibrational circular dichroism spectroscopy).

We demonstrate surface emission of terahertz (THz) frequency radiation from a monolithic quantum cascade laser with built-in control over the degree of circular polarization by "fishbone" gratings composed of orthogonally oriented aperture antennas. Different grating concepts for circularly polarized emission are introduced along with the presentation of simulations and experimental results. Fifth-order gratings achieve a degree of circular polarization of up to 86% within a 12°-wide core region of their emission lobes in the far field. For devices based on an alternative transverse grating design, degrees of circular polarization as high as 98% are demonstrated for selected far-field regions of the outcoupled THz radiation and within a collection half-angle of about 6°. Potential and limitations of integrated antenna gratings for polarization-controlled emission are discussed.

The terahertz (THz) regime of the electromagnetic spectrum contains a variety of rotational and vibrational molecular absorption lines and is thus of high interest as a fingerprint region for numerous spectroscopy and sensing applications. Quantum cascade lasers (QCLs) (1, 2) have attracted extensive research interest in recent years as highly promising sources of coherent THz radiation for such applications, and the performance of these devices has been steadily pushed forward, with recently reported peak output powers of 1 W at 10 K (3) and maximum operating temperatures as high as 200 K (4). Spectroscopy and sensing applications call for a control of the spectral and phase (5) characteristics, beam quality (6–9), and the polarization of the THz QCL device, where the latter is, for instance, of interest for vibrational circular dichroism spectroscopy. Conventionally, the intrinsically linear polarization of a facet-emitting QCL can be manipulated using external optical components such as wave plates. However, such external means of polarization manipulation are both bulky and expensive. For diode lasers, the emission of elliptically polarized radiation by monolithic devices has been achieved by injection of spin-polarized currents (10). However, external magnetic fields are required for the latter, and the degrees of circular polarization (DOCP) achieved have been very limited with values below 30% for lasers (at 50 K) (11) and below 50% for light-emitting diodes (at 290 K) (12). By hybrid integration of an external cavity diode laser with a polyimide quarter wave plate, circularly polarized emission with a high DOCP of 99% was achieved for a planar light wave circuit in ref. 13. However, up to now no monolithic, electrically pumped semiconductor laser with a high DOCP has been demonstrated.

The development of thin plasmonic-based elements (14) as an alternative for polarization control has recently attracted extensive research interest, from midinfrared quarter-wave plates (QWPs) based on antenna metasurfaces (15) to circular polarizers in the visible/near-infrared based on stacked metallic nanorods (16), among others. Efforts to integrate elements for polarization control with midinfrared QCLs have led to the demonstration of an integrated mode converter (17) [transverse magnetic (TM) to transverse electrical (TE)] and of plasmonic polarizers integrated into the facet of a QCL device (18). In the latter, the facet emission of a QCL is coupled into surface plasmons propagating along a metallic grating fabricated on the device facet, where the orientation of the grating controls the polarization state of the output radiation. The integration of two orthogonally oriented and phase-shifted gratings (a "fishbone" grating) allowed the demonstration of elliptically polarized output. However, the polarizer in ref. 18 involved patterning of the QCL facet, which cannot be achieved by photolithography but required focused-ion-beam (FIB) milling, and the fraction of the QCL output not coupling into surface plasmons led to a strong linearly polarized component in the device output.

In contrast to the dielectric waveguides conventionally used to confine the optical modes in midinfrared QCLs, THz QCLs are commonly based on single-plasmon (2) or metal–metal waveguides (19), where for both schemes the optical mode is strongly confined to the metal surface. Because of the latter, surface emitting THz QCLs can be realized by fabricating second-order gratings into the top metallization of the device (20–22). The implementation of more sophisticated metallic grating designs for THz QCLs (23) can favor laser action on the symmetric grating mode for enhanced radiation efficiency (24) and the realization of third-order gratings for low-divergence emission (25, 26).

In this work, metallic gratings for polarization-controlled surface emission from THz QCLs are demonstrated. The gratings are integrated into the top metallization of the device and are composed of sets of two orthogonal aperture antennas, similar to those used in ref. 27 for polarization-sensitive directional coupling of light to surface plasmon polaritons (SPPs). These polarizer gratings allow the efficient surface emission of THz radiation, and monolithic QCL sources of elliptically polarized THz radiation with a good degree of circular polarization are demonstrated.

RESULTS

Pre-characterization: The devices reported in this work are THz QCLs with copper metal–metal waveguides (28) lasing at wavelengths between 90 and 105 μm. Before the aperture antennas for polarization-controlled surface emission were fabricated into the top metallization, the QCLs were thoroughly precharacterized in the edge-emitting configuration to enable a comparison between the edge-emitting and the surface-emitting performance for the same device. A schematic of the experimental setup is shown in Fig. 1A, where the polarizer was not present during light-current (L-I) characterization. The broken lines in Fig. 1B show the L-I characteristics recorded during precharacterization for devices 1–5, where high-reflectivity (HR) coatings had already been applied to the device back facets. Note that the L-I characteristics are shown as measured by the bolometer and are not corrected for an estimated collection efficiency of about 0.3% for edge emission. When taking this collection efficiency into account, each of the devices reaches peak output powers between 4 and 10 mW, comparable to the QCLs reported in ref. 28. It should be mentioned that the data acquired during precharacterization allows a qualitative rather than a precise quantitative comparison between the edge emission and the power coupled out by the surface grating. A precise evaluation would require the exact determination of the collection efficiency as well as highly resolved 2D maps of the far-field intensity distribution (ideally in dependence of the driving current), which is not feasible with the used experimental setup. Following the precharacterization procedure, HR coatings were applied to the front facet of each device, effectively eliminating facet emission from the devices.

Grating Design: In this work, narrow aperture antennas in the top metallization are used to scatter radiation from a THz QCL and enable surface emission from the device. To achieve directional surface emission, the apertures are arranged in a grating configuration. The use of gratings in the surface metallization for achieving efficient surface emission is common for THz QCLs, where usually second-order gratings are used, but third- and fourth-order gratings have been demonstrated as well (25, 26). A grating of order m exhibits a periodicity of $p = m.\lambda_0/(2n_{eff})$, where λ_0 is the vacuum wavelength and n_{eff} is the effective refractive index of the mode. In case of sufficient coupling, such a grating allows constructive interference between counterpropagating modes inside the waveguide and the formation of a standing wave, as commonly exploited in distributed feedback semiconductor lasers with first-order gratings. A side-view sketch of a metal–metal waveguide with grating apertures in the top metallization is shown in Fig. 2A, where the field

amplitude of the standing wave is illustrated in black. The figure shows a fifth order grating, with a period equivalent to $p = 5.\lambda_0/(2n_{eff})$. Surface emission is possible if constructive interference by the radiation scattered from the individual grating periods occurs in the far field. In case of an even grating order, surface emission is always possible, because all grating elements are excited in phase, and the emitted radiation interferes constructively in the direction normal to the surface. For odd grating orders, neighboring grating periods are excited with a phase shift of $\Delta\Phi_b = \pi$, as illustrated in Fig. 2A. Constructive interference in the far field between waves scattered by neighboring periods is therefore only possible at finite angles α, at which this phase shift and the one accumulated during free-space propagation [$\Delta\Phi_a = 2\pi p \sin(\alpha)/\lambda_0$] satisfy the following condition for an integer l:

$$\pi + 2\pi p \sin(\alpha)/\lambda_0 = 2\pi l \qquad \textbf{[1]}$$

With $p = m.\lambda_0/(2n_{eff})$ and an effective refractive index significantly greater than 3, as is the case for the THz waveguides in this work, the lowest order enabling surface emission at an angle from an infinitely long grating is m = 5. As discussed in the following section, a significant emission angle is essential for the grating concept demonstrated in this work, and fifth-order gratings were therefore realized for the devices presented here. It should be pointed out that the order nomenclature of gratings refers to their feedback order. Now, even though the gratings demonstrated in this work did not provide sufficient feedback in the waveguide to observe significant mode-selection behavior (Fig. 1C), the order nomenclature was applied nevertheless. This choice of p is necessary to ensure a fixed phase relation between the individual grating periods and a homogenous outcoupling over the whole grating length. If the condition for p is not fulfilled, a phase flip occurs periodically, resulting in a more complex far field and a less directional emission, as discussed further below.

Each period of the presented gratings comprises several slot antennas for polarization control. A narrow aperture in a metallic film only scatters light with an electric field component perpendicular to the slot length, a feature used, for instance, in the directional plasmonic couplers in ref. 27. Thus, by selecting a certain orientation of the aperture antenna on the QCL ridge, surface emission of an arbitrarily oriented polarization with respect to the ridge direction can be achieved. Note that the polarization state of surface emission from a QCL is orthogonal to that of the TM lasing modes inside the waveguide, and that the outcoupling of TE-polarized radiation is possible owing to “field bending” caused by the apertures in the metal–metal waveguide (22). While an ensemble of parallel aperture antennas can achieve outcoupling of an arbitrarily oriented linear polarization, using two sets of orthogonally oriented apertures is a promising approach for the emission of circularly or elliptically polarized radiation, as long as a well-defined phase relation between the excitation of the two aperture sets can be implemented. In ref. 27 the authors used two rows of orthogonal aperture antennas in a gold layer forming a second-order grating for directional coupling of circularly polarized light to SPPs propagating along the metal surface. This approach is fundamentally different from that in ref. (29), which very recently reported on the directional coupling of the emission from a spherical nanoparticle to an air-clad silica nanofiber. In contrast to the nanoparticle in ref. 29 acting as a polarization maintaining scatterer, the two kinds of antennas in ref. 27 are only excited by the electric field component orthogonal to their elongation. Depending on the handedness of the incoming radiation, the two types of antennas launch SPPs with $+\pi/2$ or $-\pi/2$ phase shift with respect to each other. Because the two types of antennas are separated by a quarter of the SPP wavelength, the SPPs launched in one direction interfere constructively, whereas propagation in the other direction is suppressed by destructive interference. For a traveling electromagnetic wave in a metal–metal waveguide, an analogous scheme could be used to couple out circularly polarized light by adjusting the excitation phase between two orthogonal sets of antennas emitting with orthogonal linear polarizations. By separating the two sets of antennas by a quarter wavelength in the medium, they would emit radiation phase-shifted by $\pi/2$. However, the ridge of a THz QCL forms a resonator, and this picture of traveling waves breaks down as right- and left propagating waves form a standing wave. The electric field vectors at two different points along the cavity are either oscillating in phase or phase-shifted by π. Thus, the concept presented in ref. 27, which is based on a $\pi/2$ phase shift in the excitation of two different antennas, cannot be directly adapted to QCL cavities.

As an alternative, the grating designs realized for the devices in this work involve surface emission by two orthogonal sets of antennas oscillating in phase (or, equivalently, phase-shifted by 180°) and a subsequent accumulation of phase during free space propagation, as opposed to the phase shift in the antenna excitation itself used in ref. 27. Fig. 3A illustrates the longitudinal grating design for polarization-controlled surface emission presented in this work. Two fifth-order gratings composed of orthogonally oriented aperture antennas are shifted longitudinally with respect to each other, where the large emission angle around

44° of the grating enables the accumulation of a significant phase difference during free-space propagation and thus the control of the polarization state in the far field. To generate circularly polarized emission, the two gratings of orthogonally oriented antennas have to be shifted by half of the grating period, so that a phase difference of $\pi/2$ between the two orthogonal linearly polarized components of the emission is accumulated in the far field owing to a well-defined path difference $\Delta x = \lambda_0/4$, as sketched in Fig. 3B. However, the two different gratings are in such a case shifted by exactly a quarter wavelength in the medium. Thus, if one grating is placed at the intensity maximum of the standing wave pattern in the cavity, the antennas of the other grating are excited only weakly owing to their position in the intensity nodes. To mitigate this difficulty with coupling efficiency, an elliptically polarized output rather than circularly polarized emission was targeted in devices 2–5 of this work. By design, the two types of antennas were shifted by about three-eighths rather than half of the grating period with respect to each other.

The aperture antenna gratings were fabricated by FIB milling of openings into the top metallization of the individual devices. They are composed of 2-μm-wide and 13- to 15-μm-long apertures in the metallization, as seen in the SEM images in, for example, Fig. 3A. FIB structuring allowed a direct comparison of the device performance before and after patterning, as already mentioned above. However, it should be pointed out that owing to the large dimensions of the antenna apertures the grating designs presented here can also be realized using optical lithography and a subsequent lift-off process.

Control of Linear Polarization Direction by Slot Antennas: To first demonstrate surface emission of arbitrarily oriented linear polarization, a grating composed of only one set of equally oriented apertures was realized for device 1. For a 90-μm-wide QCL ridge, a grating composed of nine periods of 15-μm-long antennas was patterned into the top metallization, as seen in the SEM image in Fig. 2B. Each grating period comprises eight antennas, transversally separated by 10 μm to avoid coupling between neighboring antennas. The period length of the pattern is 61 μm; the antenna rows thus roughly form a fifth-order grating. The aperture antennas are oriented at an angle of 45° to the waveguide and couple to the modes inside the metal–metal cavity. The coupling between the grating and the QCL mode is expected to be too weak to provide sufficient feedback for wavelength selection owing to its short length and small overall aperture area, and no conclusive influence of the grating on the emission spectra was observed. The latter is demonstrated in Fig. 1C, which shows representative emission spectra for device 3. The red curve presents the spectrum for facet emission, recorded before applying an antireflective (AR) coating to the front facet and before FIB patterning of the top metallization. The surface emission spectrum of device 3 after FIB structuring and applying the front-facet AR coating is shown by the blue curve. Both spectra were recorded at a driving current of 2 A and show the typical multimode emission of a Fabry–Perot cavity, with slightly different spectral characteristics owing to the change in the cavity properties. The L-I characteristics for surface emission of device 1 as recorded with an aperture of 2 cm are presented in Fig. 1B (pink solid line). Note that the data are shown as measured, not corrected for collection efficiency. At the same collection half angle of 5.7° the collected output power from device 1 is a factor of four higher for surface emission than for edge emission. This is due to the more collimated far-field intensity distribution of the surface emission compared with the highly divergent facet emission (see discussion for fifth-order gratings below).

Fig. 2C presents the experimentally determined polarization state of the surface emission of device 1 in a polar plot. As predicted by finite difference time domain (FDTD) simulations, the aperture antennas couple out linearly polarized radiation with an electric field vector normal to the antenna orientation. Note that the orientation of the polar plot is consistent with that of the SEM image in Fig. 2B. The experimental data on device 1 therefore demonstrate that an aperture grating patterned into the top metallization of a metal–metal waveguide enables surface emission by a THz QCL at a selected linear polarization controlled by the antenna orientation. In the following, a combination of two gratings of different orientation is used to achieve elliptically polarized output, and in principle more sophisticated patterns of aperture antennas in the QCL metallization can generate more complex phase front states of the surface-emitted beam.

Fifth-Order Gratings for Elliptically Polarized Surface Emission: Based on the design for elliptically polarized surface emission discussed above, four surface-emitting THz QCL devices with rows of two differently oriented aperture antennas creating approximately a fifth-order grating were fabricated, where antennas of rectangular shape (2 × 15 μm) were milled into the device top metallization using the FIB. For these four fifth-order grating devices with two sets of apertures, referred to as devices 2–5, the period length and respective center wavelength of QCL emission, as well as the number of grating periods and exact shifts between the two aperture sets, are given in Table 1. Fig. 3A shows a representative top-view electron micrograph of the grating of device 2. The transverse spacing between neighboring antennas in the same row

is 10 μm for devices 3 and 4 and 20 μm for devices 2 and 5, where the increased transverse spacing for the latter aims at excluding any potential coupling between neighboring antenna elements and decreasing the writing time during FIB fabrication. The antennas of the two sets are orthogonal to each other and are oriented at an angle of 45° to the waveguide direction. Fig. 3C shows the angular far-field intensity distributions for surface emission of the fifth-order grating devices in the x–z plane. All of the four devices show a relatively broad, dual-lobed far-field distribution with peaks around ±47°. Note that the devices emit at slightly wider angles to the surface normal than expected for an ideal fifth-order grating (around 44° for n_{eff} ~3.5), which is due to a grating period slightly shorter than $2.5\lambda_0/n_{eff}$. This deviation might also be the cause for the interference fringes in the far field observed for device 5.

L-I characteristics recorded for surface emission of the fifth order devices at the maximum of the far-field distribution are presented by the solid lines in Fig. 1B. For a collection half-angle of 5.7°, all of these devices show a significantly enhanced peak power as measured by the Si bolometer in the case of surface emission by the grating, with enhancement factors of between 2.2 and 4.4 compared with the collected power for edge emission. Again, this is due to a more collimated far-field intensity distribution in case of surface emission. By assuming a diffraction limited far-field distribution for edge emission from a 100-μm-wide and 10-μm-high facet, a collection efficiency of about 0.3% is estimated. As calculated from the far-field intensity distribution for surface emission in the x–z plane (Fig. 3C) recorded by rotating the QCL, the collection efficiency increases by a factor of 13 for device 2 compared with facet emission, giving an estimated collection efficiency of 3.2% for surface emission from this device. The estimation of the collection efficiencies indicates a total surface emitted power of 17, 25, 56, and 26% of the corresponding edge-emitted power for devices 2–5, respectively. The reduced outcoupling efficiency of the surface-emitting device compared with the edge-emitting configuration is also reflected in a reduction in both the threshold current and the rollover current (point of maximum power), as seen in Fig. 1B. All of the demonstrated devices therefore feature outcoupling of THz radiation by a fifth-order grating with output powers comparable to those for edge-emitting devices even for relatively short gratings. Note that increasing the number of grating periods would increase the outcoupling efficiency, and significantly higher output powers can be achieved in future devices with lithographically defined gratings extending over the entire QCL ridge length.

Fig. 3D shows polar plots of the polarization-dependent emission of devices 2–5, obtained at the maximum of the far-field intensity distribution in Fig. 3C. Devices 2 and 3 emit elliptically polarized THz radiation with a significant degree of circular polarization, as seen from the blue and red curves in Fig. 3D and discussed in the following analysis using the Stokes vector formalism. As already mentioned, the elliptically polarized surface emission of devices 2 and 3 originates from an excitation of antenna oscillations by the TM modes of the QCL cavity, where each type of antenna emits at a linear polarization normal to its elongation, labeled pol. 1 and pol. 2 in Fig. 3B. At a fixed point in the far field, the electric field vector evolution of the emitted radiation with time t is given by $E = A.\hat{e}_1.\sin(\omega t + \varphi) + B.\hat{e}_2.\sin(\omega t + \varphi + \Delta\varphi)$, where $\hat{e}_1$ and $\hat{e}_2$ are unity vectors normal to the respective antenna elongation direction, A and B are the field amplitudes generated by the two antenna types, ω is the angular frequency of the radiation, and φ is a position-dependent phase. As mentioned above, the phase shift $\Delta\varphi$ between the two orthogonal field components is accumulated during free-space propagation of the THz radiation coupled out by the different antennas owing to the tilted emission angle with respect to surface normal. For a shift between the elements of d_0 and an emission angle of α, the designed phase difference between the two orthogonal linear polarizations accumulated owing to the path difference of Δx is given by $\Delta\varphi = 360°.\Delta x/\lambda_0 = 360°.d_0.\sin(\alpha)/\lambda_0$ = 65° (63°) for device 2 (device 3), as illustrated in the side view schematics of the waveguide in Fig. 3B. Even though a higher yield of devices with similar coupling by both antenna types is expected for the elliptical design presented compared with that for purely circular polarization, a significant difference in the coupling efficiency between the two antenna types was observed for all of the fabricated fifth-order grating devices. By fitting the experimental data in Fig. 3D, $\Delta\varphi$ = 67° (62°) and A:B = 62:37 (58:42) was obtained for device 2 (device 3), in good agreement with the designed phase shift. By relating the measured polarization-dependent intensity characteristics in Fig. 3D to the so-called polarization ellipse and further determining the respective Stokes parameters (30), DOCP values can be determined for the QCL devices. Assuming that the total degree of polarization is 100% (no unpolarized emission), the lengths of the principal semiaxes of the polarization ellipse a_0 and b_0 relate to the maximum and minimum intensity values I_{max} and I_{min} of the data presented in Fig. 3D by $a_0 = I_{max}^{1/2}$ and $b_0 = I_{max}^{1/2}$. The Stokes parameter S_3, equivalent to the difference between the intensities attributed to the two different circular polarization states, is then given by $S_3 = 2.a_0.b_0 = 2.I_{max}^{1/2}.I_{max}^{1/2}$, with the definition of the DOCP as $S_3/(I_{max} + I_{min})$. For devices 2

and 3, DOCP values of 74 and 86% are obtained, demonstrating the surface emission of elliptically polarized radiation with a high DOCP by a monolithic QCL device. Ideally (for A = B), the grating design gives a DOCP of 90%. Thus, whereas the relative phase between the two linearly polarized components matches the design values for devices 2 and 3, the control of the relative amplitude of these components is challenging, as expected and discussed above. Whereas there is a significant but tolerable difference in the coupling efficiencies between the two types of antennas for devices 2 and 3, emission from one kind of antenna is dominant for devices 4 and 5 owing to an uncontrolled positioning of the grating relative to the stationary intensity pattern inside the cavity. For devices 4 and 5, the antennas of one orientation dominate surface emission owing to their position close to the field amplitude maximum, whereas the other antenna type experiences very weak coupling owing to its position at the intensity minimum of the longitudinal field distribution. This leads to an almost linearly polarized output, as seen from the light blue and green curves in Fig. 3D.

Although the fifth-order surface gratings demonstrate that efficient elliptically polarized surface emission from a QCL can be achieved by introducing a phase shift between the radiation from two sets of orthogonal apertures fabricated into the top metallization, they also illustrate that achieving a high yield of devices with good DOCP values requires a reliably equal coupling strength between the waveguide modes and both types of antenna. In case of longitudinal gratings for polarization-controlled surface emission, this in turn calls for a precise control over the relative position of the grating with respect to the standing wave pattern inside the waveguide. This was not realized for the devices presented in this work, leading to the low observed yield of devices with a good DOCP. A precise positioning of the aperture grating with respect to the device facets, and thus to the stationary field intensity pattern, can be envisioned for future devices.

Transverse Gratings for Elliptically Polarized Surface Emission: As an alternative to longitudinal gratings, transverse grating designs are also presented here, together with their realization for THz QCL devices. To overcome the different coupling efficiencies of two types of aperture antennas owing to their placement at positions with different field amplitudes of the standing electromagnetic wave, the desired phase shift between the two orthogonally polarized emission components is accumulated owing to a free-space path difference in the transverse direction. To illustrate the transverse grating design, Fig. 4A shows an electron micrograph of the fabricated grating. The design uses a more sophisticated placing of antenna elements in both the longitudinal and transversal directions, creating an interference pattern in both dimensions. As seen in the top view of the grating, it ideally features a longitudinal period of λ_0/n_{eff}. Each period of the grating comprises two rows of antennas, which are in turn separated by $\lambda_0/(2n_{eff})$ in the longitudinal direction and shifted by an arbitrary distance d_1 between $\lambda_0/2$ and λ_0 in the transverse direction (d_1 = 80 μm in the case of device 6 in this work). Each row in turn contains two antennas of orthogonal orientation (dimensions 2 × 13 μm), again targeting the emission of orthogonally polarized THz radiation. The two kinds of antennas are transversally separated by $d_2 = d_1/2$ (40 μm for device 6). In the following, the operation of the transverse grating will be discussed, before presenting the experimental results on device 6.

In the case where the TM_{00} mode couples to the grating, longitudinally neighboring aperture rows are excited with a phase shift of π with respect to each other, thus forming a first-order grating in the longitudinal direction and suppressing surface normal emission. However, the transversal displacement between neighboring rows (80 μm) allows the accumulation of phase owing to a path difference in the transverse direction for finite transversal angles to the surface normal, and thus leads to constructive interference and surface emission at finite height angles Θ as illustrated in Fig. 4B. Owing to the transverse shift (of 40 μm) between the two sets of orthogonal antennas, the two orthogonal linearly polarized field components exhibit a phase shift of π/2 with respect to each other in the far-field at the emission angle Θ, and circularly polarized emission from the grating is expected.

Fig. 4C and D show plots of the calculated far-field intensity distribution for the outcoupling of the TM_{00} mode by the transverse surface grating, obtained from FDTD simulations as described in Methods. The simulation predicts a dual-lobed far-field intensity distribution with broad intensity peaks around $\pm\alpha = 30°$ in the y–z plane. Fig. 4C shows an intensity contour plot of the far-field projection of the simulated emission from the transverse grating in polar coordinates for the left-handed circularly polarized field component, and Fig. 4D shows the respective plot for the right-handed component. Note that the orientation of the far-field plot is consistent with that of the grating image in Fig. 4A. As seen from Fig. 4C and D, the surface emission of the transverse grating excited by the TM_{00} mode is therefore circularly polarized, with left-handed and right-handed emission at azimuthal angles Φ of 90° and 270°, respectively. Because the two different antenna types are positioned symmetrically in the transverse direction the coupling efficiency for both linear

polarizations is the same, and ideally perfect CP emission can be expected because both components of the electric field have equal scattering amplitude. However, there are several aspects of a real QCL device that are absent from the FDTD model used, including the gain in the material, the cavity enforcing a standing wave, and coupling between different transverse modes, all of which can lead to a deviation of device operation from the simulated characteristics. A discussion of the influence of higher-order transverse modes on the grating operation is given in Supporting Information.

Fig. 5A shows the measured far-field intensity distribution of the emission from the transverse grating of device 6 in the y–z plane, obtained by rotating the device around an axis parallel to the ridge and thus varying the altitude angle Θ at a fixed azimuthal angle of $\Phi = \pm 90°$ (for an illustration of the angle nomenclature see Fig. 4). A broad far-field distribution was observed, showing several fringes deviating from the far-field pattern expected for excitation of the grating by the TM_{00} mode as seen in Fig. 4C and D, which indicates outcoupling of higher-order modes. The polarization state of the surface emission of device 6 was determined as a function of the emission direction. As indicated by the small polar plots in Fig. 5A, the polarization state of the emitted THz radiation strongly depends on the emission angle. The far-field intensity peaks around ±10° are elliptically polarized with a high DOCP, whereas the output around 0° and around the global maximum at 34° is linearly polarized, a behavior that strongly deviates from that of the simulated emission for excitation of the grating by the TM_{00} mode as shown in Fig. 4C and D. An interpretation of this deviation will be given below.

The elliptically polarized surface emission around ±10°, which is highlighted by the polar plots in Fig. 5C, can be associated with transverse waveguide modes that strongly excite the antennas close to the ridge edges and couple weakly or negligibly to the antennas closer to the center of the ridge, as illustrated in Fig. 6A and B. This is the case for the TM_{20} mode, and Fig. 6C and D show the respective simulated far-field intensity distributions for the right and left-handed circularly polarized components. The two outer antenna sections close to the waveguide edge are transversally separated by 120 μm, and the phase difference accumulated at an emission angle of $\beta = 11°$ is 86°. This leads to the emission of radiation with a high DOCP at finite angles close to the surface normal, as predicted by the simulation results in Fig. 6C and D and observed for device 6. Fitting the polar plot of the polarization dependence in Fig. 5C as described above gives $\Delta\varphi = 87°$ (83°) and A:B = 55:45 (58:42) for emission angles of 10° and −10°, respectively. By calculating the DOCP for device 6 at 10° and −10°, values as high as 98% and 92% are obtained, respectively. To confirm that the surface emission of device 6 at an angle of 10° is truly elliptically polarized and not just an incoherent mix of linear polarizations, or put differently, that there is no significant unpolarized component rendering the determination of the DOCP as given above invalid, a commercial quartz QWP designed for a wavelength of 90 μm was placed in front of the analyzing wire-grid polarizer (at the position of the aperture in Fig. 1A). As shown by the green broken curve in Fig. 5C, the QWP completely converts the elliptically polarized output of device 6 around $\Theta = 10°$ into linearly polarized radiation, clearly demonstrating the purely elliptical polarization state with a high DOCP of the device emission within an emission half-angle of 5.7°.

Whereas the linearly polarized output of device 6 around 0° as shown by the small plot in Fig. 5A is expected owing to the vanishing optical path difference between the emission of the two types of antenna, the linear polarization state of the emission around 34° deviates from the polarization properties expected for the grating design. There are two possible explanations for this behavior. One probable cause is emission from the sidewalls of the QCL ridge, as indicated by FDTD simulations of a waveguide without sidewall metallization (Methods). This might result in a more complex interference pattern with the top emission and an uncontrolled phase relation between the different linearly polarized field components, where the side emission is predicted to be more pronounced for higher-order transverse modes. However, the resulting additional losses are also expected to suppress lasing on higher-order modes in such a scenario. The second potential cause is phase locking of different higher-order transverse modes (31, 32). For further discussion of the latter see Supporting Information. Note that although the position of bonding wires can strongly influence the far-field of surface emitting THz QCLs, such an effect is a rather unlikely explanation for the discussed deviation of the device performance from the expected behavior. In contrast to the direct bonding to the patterned top metallization in ref. 33 the bonding wires were applied to the unpatterned metallization section of the devices demonstrated here and lead to the chip carrier pads without crossing above the antenna segment.

The L-I-characteristics of the elliptically polarized surface emission of device 6 are shown in Fig. 5B for emission angles of 10° and −10° by the blue and red curves, respectively, in comparison with the edge-

emitting characteristics represented by the broken black curve. Again, for the same collection half-angle of 5.7° the surface emission exceeds the edge emission by a factor of 1.8 in power at the detector owing to the more collimated output from the grating.

In summary, even though the presented experimental results on a transverse grating in the top metallization of a THz QCL demonstrate that surface emission of elliptically polarized radiation with a high DOCP can be achieved around particular emission angles, the data also indicate that the operation of such a transverse grating for polarization-controlled outcoupling is influenced by lasing on higher-order transverse modes. As a consequence, only a fraction of the outcoupled power exhibits an elliptical polarization state with a good DOCP, and the output outside of a limited emission half-angle of 5.7° has to be blocked during employment as a circularly polarized source. Achieving reliable surface emission of circularly polarized radiation in combination with a clean, dual-lobed far-field emission profile for a circular polarization state of the total output power in future devices requires efficient suppression of lasing on higher order lateral modes. The latter was achieved in ref. 34 for a THz QCL with metal–metal waveguide by introducing side absorber regions causing high losses for higher-order transverse modes, a concept that could be implemented during the same lithographic step defining the aperture antennas in future devices.

CONCLUSION

In conclusion, we have demonstrated surface emission of elliptically polarized radiation from THz QCLs by integrating orthogonally oriented aperture antennas into the top metallization of a metal–metal waveguide. Good outcoupling efficiencies for different kinds of surface gratings with estimated ratios between the total surface-emitted power and the edge-emitted power above 17% are reported for gratings stretching over less than half of the total QCL ridge length, where the grating length was limited by stitching errors and writing time of the FIB milling process. Coverage of the whole ridge can be achieved by photolithographic definition of the grating in future devices. Different grating concepts have also been realized, enabling the emission of arbitrarily linearly polarized radiation as well as an elliptically polarized output from monolithic QCL devices. Good degrees of circular polarization have been achieved for individual far-field lobes of the surface emission from a THz QCL within limited emission half-angles of 5.7°. For a transverse grating of 220 μm length, 50 μW of output power with a degree of circular polarization as high as 98% was collected within a half-angle of 5.7°. With additional design elements for controlling the relative position of longitudinal gratings with respect to the standing wave pattern in the cavity, or for suppressing lasing on higher-order transverse modes in future devices, gratings for polarization-controlled surface emission are highly promising for the realization of monolithic sources of purely circularly polarized radiation for spectroscopic applications in the THz as well as the midinfrared regions.

METHODS

Device Fabrication: The QCL material was based on a three-well resonant-phonon active region design (35) and was grown by molecular beam epitaxy on an undoped GaAs substrate. It was processed into copper metal–metal waveguides of different widths as outlined in ref. 28. After cleaving the waveguides into 1.2- to 1.7-mm-long devices, the chips were mounted on a copper heat sink. An HR coating composed of 150 nm of Al_2O_3, 10 nm of Ti, and 100 nm of Au was then applied to the back facet of the chips. After pre-characterization of the Fabry–Perot laser devices, facet emission was eliminated by covering the front facet by an HR coating. The antenna gratings for polarization-controlled surface emission were fabricated into the top metallization of the QCLs by FIB milling. Note that FIB milling was used as a highly flexible patterning method to allow the grating fabrication on fully processed and precharacterized QCL devices, which enables the direct comparison between the edge- and surface-emitting performances for the same laser ridge.

Simulations: The far-field characteristics and polarization states expected for surface emission from the various grating designs were calculated by FDTD simulations of a TM_{00} mode traveling along a metal–metal waveguide of cross-sectional dimensions equivalent to those of the respective device and with the aperture grating integrated in the top metallization. To illustrate the ideal performance of the transverse grating realized for device 6, the sidewalls of the waveguide in the model were covered by copper, preventing radiation scattered by the antenna elements from exiting the waveguide via the ridge sidewall. For an uncovered waveguide sidewall, the simulation predicts a significant influence of the side-emitted radiation on the far-field pattern and polarization state of device emission. Because the predicted side emission is far more pronounced for higher-order modes than for the TM_{00} mode, the resulting additional losses are expected to influence the mode selection in a real device. However, the full modeling of the influence of the

grating on the mode selection is beyond the scope of this work. Thus, the simulation plots presented here serve the purpose of illustrating the ideal operation of the transverse grating in the absence of side emission and help to interpret physically specific experimental observations rather than account for the complete device performance.

Measurements: For all of the experimental results presented here the devices were placed in a cryostat and cooled down to liquid-nitrogen temperature (78 K). The devices were operated in pulsed mode at a repetition rate of 10 kHz and a pulse length of 100 ns, giving a duty cycle of 0.1%. In addition, the pulse generator was gated by a 473-Hz signal with 50% duty cycle to allow measurements in a lock-in configuration. The emission of the devices was collected by a parabolic mirror (diameter 5 cm, focal length 10 cm) at a distance of 10 cm, giving a maximum f-number of 2, and focused onto a helium cooled silicon bolometer by a second parabolic mirror. To reach a higher angular resolution for the far-field scans recorded for this work the collection angle was further reduced by placing an aperture of 2 cm diameter between the two parabolic mirrors, increasing the collection f-number to 5 for all of the experimental results shown. Note that the estimates for the collection efficiency of the setup given in the main text for edge-emitting devices were obtained by assuming lasing of the TM_{00} mode and calculating the corresponding diffraction-limited emission angle. Lasing on higher-order lateral modes, which is indicated for device 6, might lead to an overestimation of the collection efficiency. The far-field intensity distribution of the QCLs with fifth-order gratings was characterized by rotating the devices around an axis on the device plane and normal to the ridge elongation, thus sweeping the emission angle as sketched in Fig. 1A. The far-field characteristics of the transverse grating device were obtained by rotating the QCL around an axis parallel to the ridge. The collection half-angle of 5.7° limits the resolution of the far-field data. To compensate for a tilt in the sample mounting and misalignments of the cryostat, the zero-angle position of the far-field profiles obtained was calibrated to coincide with the center between the two intensity peaks. The polarization state of the surface emission was characterized by placing a polyethylene wire-grid polarizer into the parallel beam between the two parabolic mirrors of the setup, as shown in Fig. 1A, and by recording the bolometer signal as a function of the polarizer orientation while rotating the latter. The orientation of the wire-grid polarizer was calibrated using a facet emitting QCL. The polarizer had a clear aperture of 2 cm and therefore did not change the collection f-number of the setup. The polarization-dependent data were recorded for a half-circle of polarizer rotation only in most cases (the polarizer orientation γ is ideally equivalent to $\gamma + \pi$) and were then plotted twice over the whole circle to give a more intuitive presentation.

ACKNOWLEDGMENTS

The authors acknowledge the Center for Nanoscale Systems (CNS) at Harvard University, a member of the National Nanotechnology Infrastructure Network. We thank Nicholas Antoniou of Harvard CNS for his excellent support during focused-ion-beam structuring. We are grateful for support from the Engineering and Physical Sciences Research Council and the European Research Council program TOSCA (Terahertz Optoelectronics – From the Science of Cascades to Applications). A.G.D. acknowledges support from the Royal Society and Wolfson Foundation. P.R. acknowledges support from the Austrian Science Fund (Fonds zur Förderung der wissenschaftlichen Forschung, project J 3092-N19).

REFERENCES

1. Faist J, et al. (1994) Quantum cascade laser. Science 264(5158):553–556.
2. Köhler R, et al. (2002) Terahertz semiconductor-heterostructure laser. Nature 417(6885):156–159.
3. Li L, et al. (2014) Terahertz quantum cascade lasers with >1 W output powers. Electron Lett 50(4):309–311.
4. Fathololoumi S, et al. (2012) Terahertz quantum cascade lasers operating up to ~ 200 K with optimized oscillator strength and improved injection tunneling. Opt Express 20(4):3866–3876.
5. Burghoff D, et al. (2014) Terahertz laser frequency combs. Nat Photonics 8:462–467.
6. Sirtori C, Barbieri S, Colombelli R (2013) Wave engineering with THz quantum cascade lasers. Nat Photonics 7:691–701.
7. Yu N, Capasso F (2010) Wavefront engineering for mid-infrared and terahertz quantum cascade lasers. J Opt Soc Am B 27(11):18–35.
8. Scalari G, et al. (2009) THz and sub-THz quantum cascade lasers. Laser Photon Rev 3(1-2):45–66.
9. Kumar S (2011) Recent progress in terahertz quantum cascade lasers. IEEE J Sel Top Quant Electron 17(1):38–47.

10. Holub M, Bhattacharya P (2007) Spin-polarized light-emitting diodes and lasers. J Phys D Appl Phys 40(11):R179.
11. Holub M, Shin J, Saha D, Bhattacharya P (2007) Electrical spin injection and threshold reduction in a semiconductor laser. Phys Rev Lett 98(14):146603.
12. Jiang X, et al. (2005) Highly spin-polarized room-temperature tunnel injector for semiconductor spintronics using MgO(100). Phys Rev Lett 94(5):056601.
13. Kim RK, et al. (2007) Circularly polarized external cavity laser hybrid integrated with a polyimide quarter-wave plate on planar lightwave circuit. IEEE Photon Technol Lett 19(14):1048–1050.
14. Yu N, et al. (2011) Light propagation with phase discontinuities: Generalized laws of reflection and refraction. Science 334(6054):333–337.
15. Yu N, et al. (2012) A broadband, background-free quarter-wave plate based on plasmonic metasurfaces. Nano Lett 12(12):6328–6333.
16. Zhao Y, Belkin MA, Alù A (2012) Twisted optical metamaterials for planarized ultrathin broadband circular polarizers. Nat Commun 3:870.
17. Dhirhe D, Slight TJ, Holmes BM, Hutchings DC, Ironside CN (2012) Quantum cascade lasers with an integrated polarization mode converter. Opt Express 20(23):25711–25717.
18. Yu N, et al. (2009) Semiconductor lasers with integrated plasmonic polarizers. Appl Phys Lett 94(15):151101.
19. Unterrainer K, et al. (2002) Quantum cascade lasers with double metal-semiconductor waveguide resonators. Appl Phys Lett 80(17):3060–3062.
20. Demichel O, et al. (2006) Surface plasmon photonic structures in terahertz quantum cascade lasers. Opt Express 14(12):5335–5345.
21. Fan JA, et al. (2006) Surface emitting terahertz quantum cascade laser with a doublemetal waveguide. Opt Express 14(24):11672–11680.
22. Kumar S, et al. (2007) Surface-emitting distributed feedback terahertz quantumcascade lasers in metal-metal waveguides. Opt Express 15(1):113–128.
23. Mahler L, Tredicucci A (2011) Photonic engineering of surface-emitting terahertz quantum cascade lasers. Laser Photon Rev 5(5):647–658.
24. Xu G, et al. (2012) Efficient power extraction in surface-emitting semiconductor lasers using graded photonic heterostructures. Nat Commun 3:952.
25. Amanti MI, Fischer M, Scalari G, Beck M, Faist J (2009) Low-divergence single-mode terahertz quantum cascade laser. Nat Photonics 3:586–590.
26. Kao T-Y, Hu Q, Reno JL (2012) Perfectly phase-matched third-order distributed feedback terahertz quantum-cascade lasers. Opt Lett 37(11):2070–2072.
27. Lin J, et al. (2013) Polarization-controlled tunable directional coupling of surface plasmon polaritons. Science 340(6130):331–334.
28. Belkin MA, et al. (2008) Terahertz quantum cascade lasers with copper metal-metal waveguides operating up to 178 K. Opt Express 16(5):3242–3248.
29. Petersen J, Volz J, Rauschenbeutel A (2014) Nanophotonics. Chiral nanophotonic waveguide interface based on spin-orbit interaction of light. Science 346(6205):67–71.
30. Yariv A, Yeh P (2007) Photonics: Optical Electronics in Modern Communications (Oxford Univ Press, New York), 6th Ed, pp 21.
31. Bewley WW, et al. (2005) Beam steering in high-power cw quantum-cascade lasers. IEEE J Quantum Electron 41(6):833–841.
32. Yu N, et al. (2009) Coherent coupling of multiple transverse modes in quantum cascade lasers. Phys Rev Lett 102(1):013901.
33. Chassagneux Y, et al. (2009) Electrically pumped photonic-crystal terahertz lasers controlled by boundary conditions. Nature 457(7226):174–178.
34. Fan JA, et al. (2008) Wide-ridge metal-metal terahertz quantum cascade lasers with high-order lateral mode suppression. Appl Phys Lett 92(3):031106.
35. Luo H, et al. (2007) Terahertz quantum-cascade lasers based on a three-well active module. Appl Phys Lett 90(4):041112.

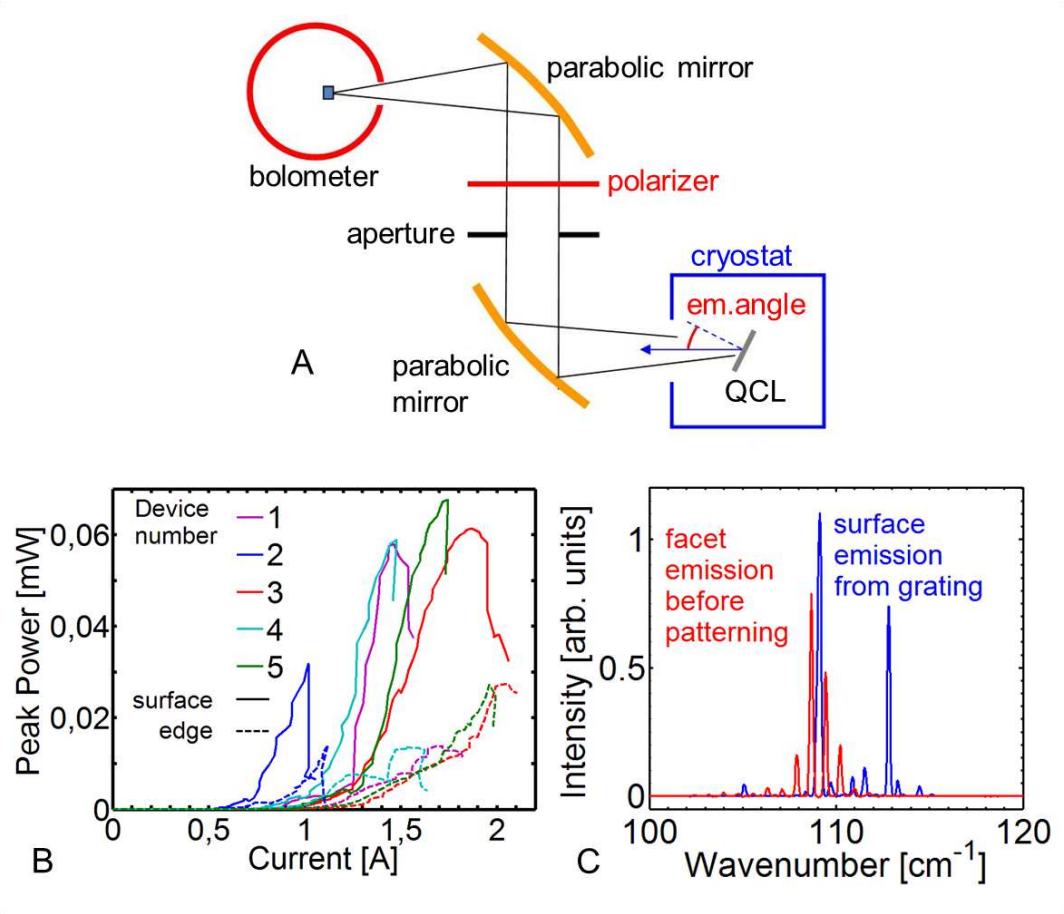

Fig. 1. Performance before and after grating fabrication.
(A) Schematic (not to scale) of the experimental setup used for device characterization.
(B) Light current characteristics of devices 1–5 for surface emission (solid lines) and for edge emission (broken lines). The edge-emission data for each device were acquired after applying an HR coating to the back facet and before grating fabrication. The surface emission characteristics were measured for the same device after covering the front facet by an HR coating and after grating fabrication. The data are shown as measured and not corrected for the collection efficiency.
(C) Representative emission spectra for device 3 at a current of 2 A before (red curve) and after (blue curve) grating fabrication. Both spectra show typical Fabry–Perot characteristics; no conclusive influence of the gratings on the mode selection was observed for the devices.

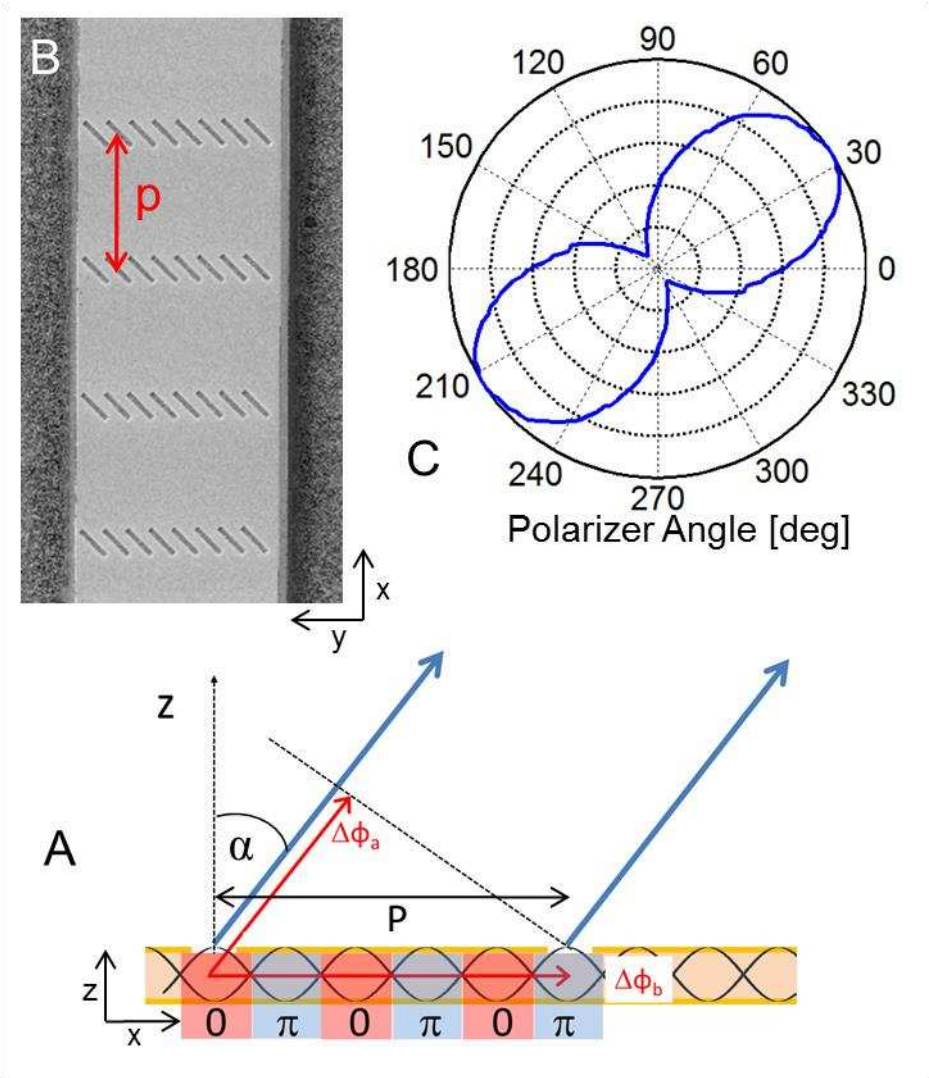

Fig 2. Layout and polarization state of a surface-emitting laser with antenna controlled linear polarization (device 1).
(A) Side-view illustration of the surface emission condition for a fifth-order grating in the top metallization of a metal–metal waveguide. Neighboring grating apertures are excited with a phase shift $\Delta\Phi_b = \pi$ by the standing wave inside the cavity. To achieve constructive interference in the far-field at an angle α, this phase shift has to be compensated during free-space propagation by the phase shift $\Delta\Phi_a$.
(B) Top-view electron micrograph of the aperture antenna grating for surface emission in the top metallization of device 1.
(C) Polar plot of the polarization-dependent output power of device 1 measured by rotating a linear polarizer in front of the detector. The surface emission is linearly polarized at an angle determined by the orientation of the grating antennas.

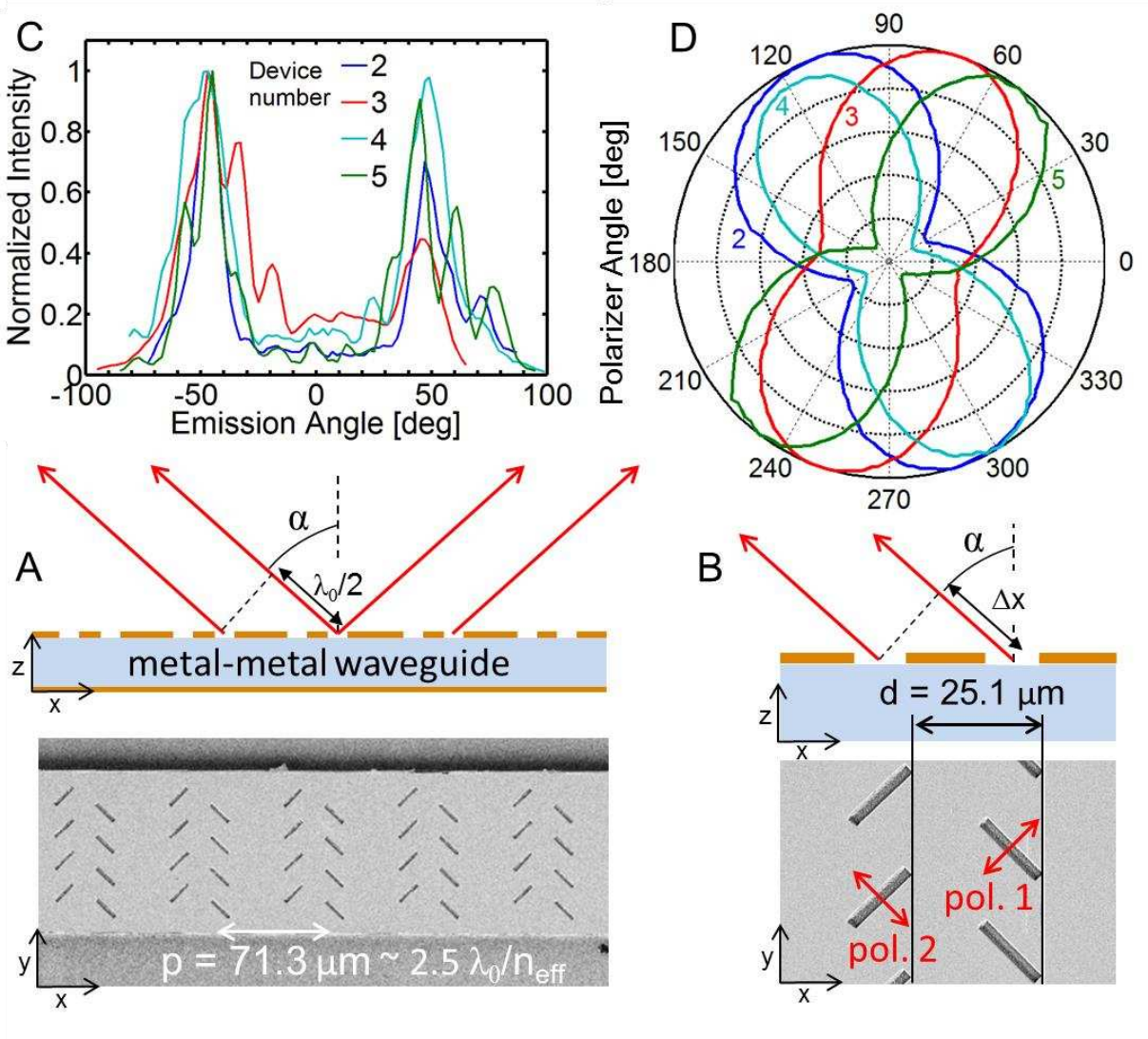

Fig 3. Layout and operation of the fifth-order gratings.
(A) Top-view electron micrograph of the fifth-order grating layout of device 2, representative for the design of devices 2–5, together with a side-view sketch illustrating constructive interference in the far field at an angle of $\pm\alpha$.
(B) Illustration of the phase shift between the linearly polarized emission from the two types of antennas based on a path difference of Δx during free-space propagation at an emission angle of α in the x–z plane, leading to the elliptical polarization characteristics in D.
(C) Measured angular far-field intensity distribution in the x–z plane of the emission from devices 2–5, showing two lobes around ±47°.
(D) Normalized polar plot of the polarization-dependent output power of the fifth-order grating devices, measured at the intensity maximum of the far-field distribution with a collection half-angle of 5.7°. The curves are labeled by the device number. Devices 2 and 3 feature elliptically polarized emission with degrees of circular polarization of 74% and 86%, respectively.

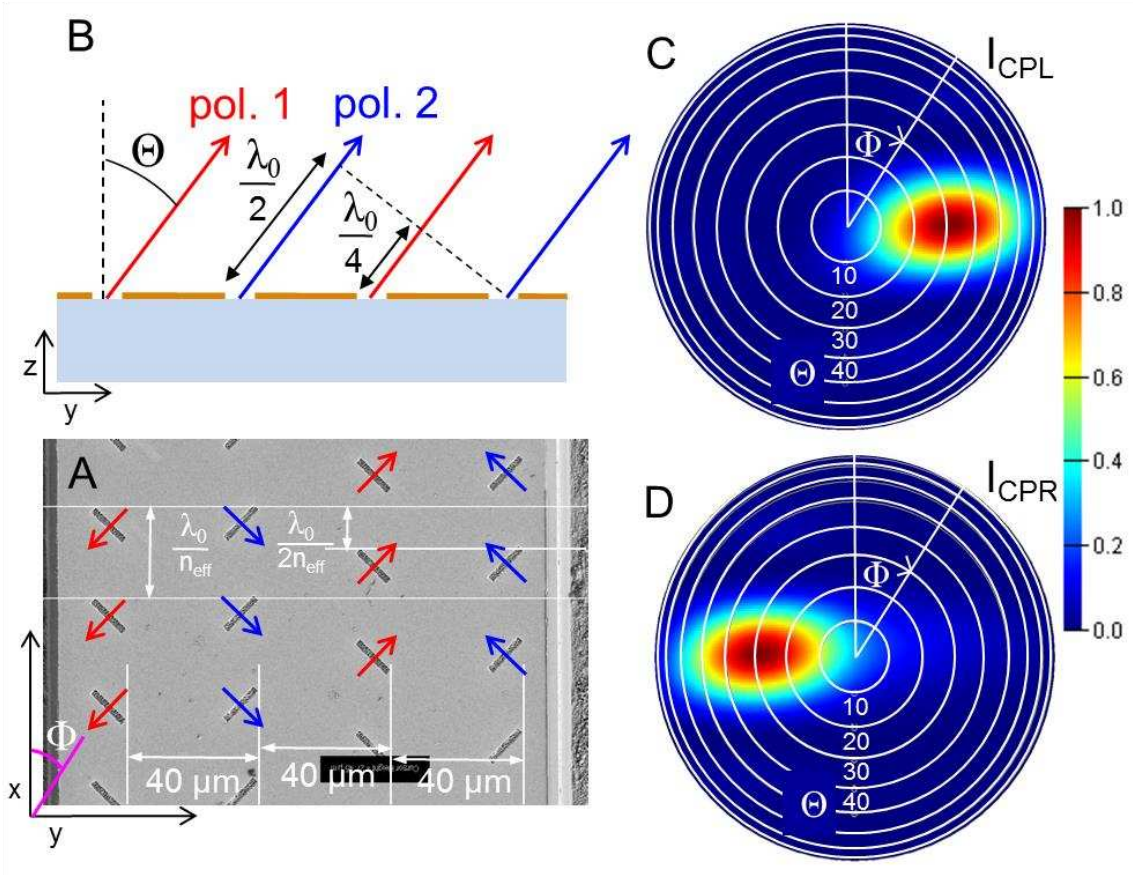

Fig 4. Layout and ideal operation of the transverse antenna grating.
(A) Top-view electron micrograph of the antennas in the top metallization of device 6, together with an illustration of both the linear polarization state and the relative phase of the radiation emitted by the two antenna types for excitation by the TM_{00} waveguide mode.
(B) Side-view sketch illustrating constructive interference in the far-field at $\pm\Theta$ in the y–z plane for antenna excitation by the TM_{00} mode, as well as a phase shift of $\pi/2$ between the two linear polarizations 1 and 2.
(C) Contour plot in polar coordinates of the far-field intensity distribution of the right-handed circularly polarized component of the surface emission from the transverse grating, as calculated by FDTD simulations in the waveguide geometry.
(D) Analogous plot for the left-handed circularly polarized component. Note the high degree of circular polarization of the simulated surface emission from the transverse grating for TM_{00} excitation, where radiation of left-handed and right-handed polarization is emitted at azimuthal angles of Φ of 90° and 270°, respectively.

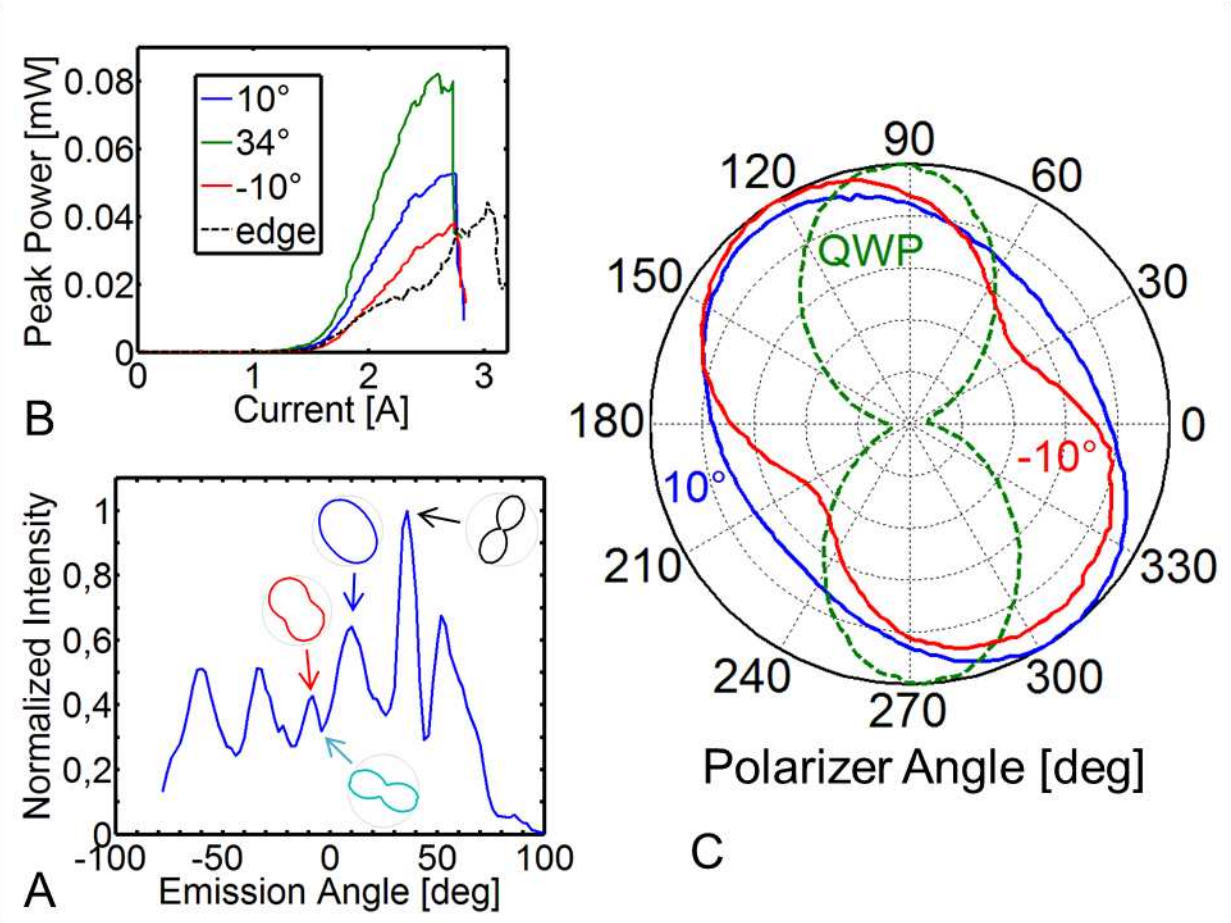

Fig. 5. Experimental results for the transverse antenna grating of device 6.
(A) Measured angular far-field intensity distribution of emission in the y–z plane, showing a broad intensity distribution with several fringes. The small insets indicate the polarization state of the respective far-field lobes.
(B) Light-current characteristics of the surface emission at different emission angles in the y–z plane, in comparison with the edge-emission characteristics recorded during precharacterization (broken line). The characteristics are not corrected for collection efficiencies of between 0.4% and 2.8% (see text).
(C) Normalized polar plot of the polarization-dependent output power of the transverse grating device, measured at angles of ±10° in the y–z plane with a collection half-angle of 5.7°. At 10° (blue curve) the collected emission exhibits a degree of circular polarization of 98%, confirmed by the broken green curve recorded with an additional quarter-wave plate in front of the analyzing wire-grid polarizer, which completely converts the elliptically polarized output into linear polarization.

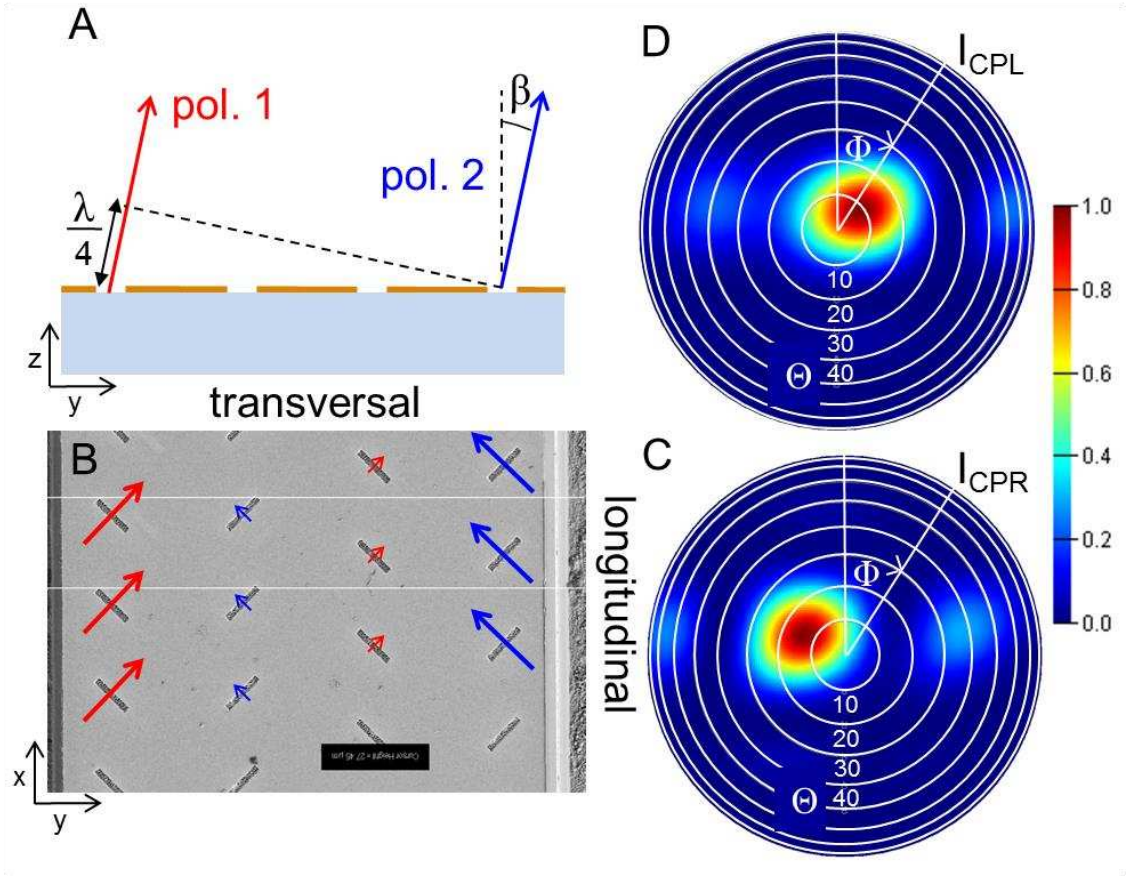

Fig. 6. Simulated outcoupling of the TM20 mode by the antenna grating.
(A) Side- and (B) top-view illustration of the excitation of the transverse grating by the TM_{20} mode, which couples strongly to the antennas close to the waveguide edge but weakly to the central rows owing to the intensity nodes of the mode. A broad far-field pattern centered around the surface normal is expected owing to the absence of strong interference. Conditions for a $\pi/2$-phase shift between polarizations 1 and 2 are illustrated in A.
(C) Contour plot in polar coordinates of the far-field intensity distribution of the right-handed circularly polarized component of the surface emission fromthe transverse grating, as calculated for the TM_{20} mode.
(D) Analog plot for the left-handed circularly polarized component. Note the high degree of circular polarization at an angle of ±11° in the y–z plane, in agreement with experimental observations for the surface emission of device 6 as shown in Fig. 5.

Table 1. Ridge and grating parameters for the realized devices along with the measured peak wavelengths

Device No.	Peak Wave-length [µm]	Ridge width [µm]	Grating			
			Period length [µm]	No. of grating periods	No. of antennas per period	Shift [µm]
1	93	90	61	9	8	-
2	102	100	71.3	9	8	25
3	92	100	58.8	9	16	22
4	91	100	63	5	16	24
5	99	130	69	5	10	26
6	98	150	27.3	9	4	-

The shift values show the longitudinal spacing between the two orthogonal antenna elements of each period. Device 6 features a more complex transverse grating (discussed in Transverse Gratings for Elliptically Polarized Surface Emission).